Microchemical Journal 191 (2023) 108899

Contents lists available at ScienceDirect

Microchemical Journal

journal homepage: www.elsevier.com/locate/microc

Study of the photobleaching phenomenon to optimize acquisition of 3D and 4D fluorescence images. A special scenario for trilinear and quadrilinear models

Adrián Gómez-Sánchez [a,b,*], Iker Alburquerque Alvarez [a], Pablo Loza-Alvarez [c], Cyril Ruckebusch [b], Anna de Juan [a,*]

[a] Chemometrics Group, Universitat de Barcelona, Diagonal, 645, 08028 Barcelona, Spain
[b] LASIRE – Laboratory of Advanced Spectroscopy, Interactions, Reactivity and Environment Université Lille, CNRS, UMR 8516, Cité Scientifique, Bâtiment C5, 59000 Lille, France
[c] ICFO-Institut de Ciències Fotòniques, The Barcelona Institute of Science and Technology, 08860 Castelldefels, Barcelona, Spain

ARTICLE INFO

Keywords:
Hyperspectral imaging
Fluorescence imaging
Multivariate Curve Resolution
Trilinear and quadrilinear models
Vegetal tissues
Rice root

ABSTRACT

Emission (3D) and excitation-emission (4D) fluorescence images allow covering wide excitation and emission spectral ranges and, hence, provide very complete information for a good characterization and location of fluorophores in samples. However, when the acquisition time of the image is too long, degradation of the fluorescence signal of compounds and sample photodamage can occur due to photobleaching. This phenomenon is due to the long exposure time of the sample to the light source and can hinder the detection and the proper characterization of the fluorophores in samples.

The main purpose of this research is providing a methodology to obtain and interpret the information of fluorescence images for the characterization of samples without suffering the consequences of photobleaching. Such a goal implies a first thorough knowledge of the photobleaching phenomenon to adapt the fluorescence imaging measurement for an optimal characterization of the fluorophores present in samples.

The proposed approach relies first on a study of time-series of 3D or 4D fluorescence images to characterize spatially and spectroscopically the fluorophores present in the samples and their photobleaching behaviour. Since photobleaching is fluorophore-dependent, the unmixing algorithm Multivariate Curve Resolution-Alternating Least Squares (MCR-ALS) is applied to the set of fluorescence images acquired as a function of time to understand the specific behaviour of every fluorophore. The characteristics of the photobleaching phenomenon and the nature of the fluorescence measurement offer a challenging scenario to look for adapted implementations of trilinear and quadrilinear models within the MCR framework. From the results obtained, appropriate instrumental settings are adopted for an image acquisition that allows the correct spatial and spectroscopic characterization of fluorophores in samples.

To test the potential of this methodology, the characterization of thin cross-sections of the *Oryza sativa* (commonly called rice) root have been studied due to the co-occurrence of several natural fluorophores in vegetal tissues.

1. Introduction

Hyperspectral imaging is a powerful analytical technique that provides spectral and spatial information of the sample surface. Each pixel of a hyperspectral image (HSI) is related to spectral information and imaging platforms are adapted to work with many spectrophotometric techniques. Hyperspectral imaging is used in many research fields, such as food quality [1,2], medicine [3–5], pharmacy [6–8] por biology [9–11]. Within the spectroscopic techniques adopted in imaging systems, fluorescence offers a high sensitivity to detect low concentrations of fluorophore compounds and the capability to provide a very detailed information on the distribution of these compounds on the sample surface due to its high spatial resolution, which can go down to several tens of nm if super resolution imaging techniques are used [12–14].

* Corresponding authors.
E-mail addresses: aderegomez@gmail.com (A. Gómez-Sánchez), anna.dejuan@ub.edu (A. Juan).

https://doi.org/10.1016/j.microc.2023.108899
Received 5 April 2023; Received in revised form 19 May 2023; Accepted 21 May 2023
Available online 22 May 2023

Confocal fluorescence microscopy can provide 3D or 4D fluorescence HSI depending on the spectroscopic information recorded [15]. Thus, a 3D fluorescence image acquires a full emission spectrum per each pixel of the sample surface at a fixed excitation wavelength, providing three-dimensional data (x, , λ). Instead, a 4D fluorescence image associates a full 2D excitation/emission landscape to every pixel, covering a range of excitation and emission wavelengths, providing four-dimensional data (x, y, λ_{ex}, λ_{em}). The combined use of 3D and 4D fluorescence images provides information on a wide spectral range of excitation and emission wavelengths and, therefore, allows an accurate sample characterization [15]. However, issues related to the instrumental image settings and to the big size of image data need to be addressed, as explained below.

The acquisition time of a 4D fluorescence HSI is relatively long. As a consequence, the degradation of the fluorescent signal of the compounds by photobleaching can occur [16]. Thus, photobleaching can hinder the detection and proper characterization of fluorophores in samples. In the worst scenario, a sample can be damaged due to laser exposition, making impossible the acquisition of images of living tissues. Hence, this phenomenon needs to be studied by collecting consecutive images as a function of time and studying the intensity decay of each fluorophore in the sample, instead of the global intensity decay. This kind of preliminary study is necessary to obtain suitable settings that enable a proper fluorescence image acquisition for sample characterization.

Understanding the information offered by fluorescence images requires chemometric tools due to the large size and complexity of the data sets acquired. Both for the study of the photobleaching phenomenon and the subsequent characterization of samples, it is relevant unmixing the raw signal into the contributions of the pure fluorophores in the samples analyzed. A solution to this problem is provided by the Multivariate Curve Resolution – Alternating Least Squares (MCR–ALS) method [17] that works iteratively decomposing the raw HSI into the pure spectral signatures and concentration maps of the image constituents. Such a procedure can work analyzing a single image or an ensemble of related images in a multiset fashion. Besides, the flexibility in data configuration allows handling 3D and 4D images [15]. The profiles issued from MCR-ALS provide a complete chemical, semiquantitative and distributional characterization of the fluorophores present in the samples and an additional description of the individual decay behavior of every fluorophore when photobleaching is investigated.

In the present work, the image acquisition protocol assisted by MCR-ALS, adapted to study photobleaching and to handle the specificities of 3D and 4D fluorescence HSI, is tested on samples of cross sections of *Oryza sativa* (rice) root. This example is a perfect testing scenario since vegetal tissues contain many natural fluorophores colocalized across the sample surface analyzed. In the following sections, the protocol to acquire and interpret images obtained in photobleaching and characterization studies is described, together with the most important results related to the specific study of *Oryza Sativa* root cross-sections.

2. Experimental work

2.1. Plant growth and sample preparation

Rice plants were grown as in Ref. [15]. After harvest, thin cross sections of roots were manually cut and placed on a 1 mm-thickness CaF2 slide with a drop of phosphate-buffered saline solution, covered with a 0.5 mm-thickness CaF2 coverslip and sealed with nail polish, to avoid water evaporation during the experiment. Fig. 1 shows the structure of a cross section of *Oryza sativa* root with the different parts identified [18].

2.2. Image acquisition

All images were collected using a Leica TCS SP8 STED 3X microscope (Leica Microsystems, Mannheim, Germany) with an HC PL APO CS2 10 × /0.40 DRY objective. The instrumental parameters were set, as explained below, depending on the experiment (photobleaching on 3D images, photobleaching on 4D images and characterization images).

For studying the photobleaching on 3D images, a 405 nm excitation laser (power of 89 μW at the sample plane) was selected with an emission range from 432.5 to 597.5 nm. The sampling interval and bandwidth were 5.69 nm with a dwell time set 3.8 μs. Six consecutive images of the same root cross-section were acquired to study the photobleaching phenomenon covering an interval of time going from 0 to 40 min. The total acquisition time of every 3D image is eight minutes. The 3D images were split in two regions of interest (ROIs): the epidermis and the stele, sized 428 × 315 μm^2 and 270 × 315 μm^2 respectively.

On the other hand, for studying the photobleaching on 4D images, a supercontinuum white light laser (WLL) was used. The excitation range covered 470 to 582 nm with a sampling interval of 8 nm (power of 146 μW at the sample planned). The emission range covered 504–624 nm with a sampling interval and bandwidth of 6 nm. The dwell time was set to 7.7 μs. Three consecutive images of the same root cross-section were acquired to study the photobleaching across the images covering an interval of time going from 0 to 24 min. The total acquisition time of every 4D image is 12 min.

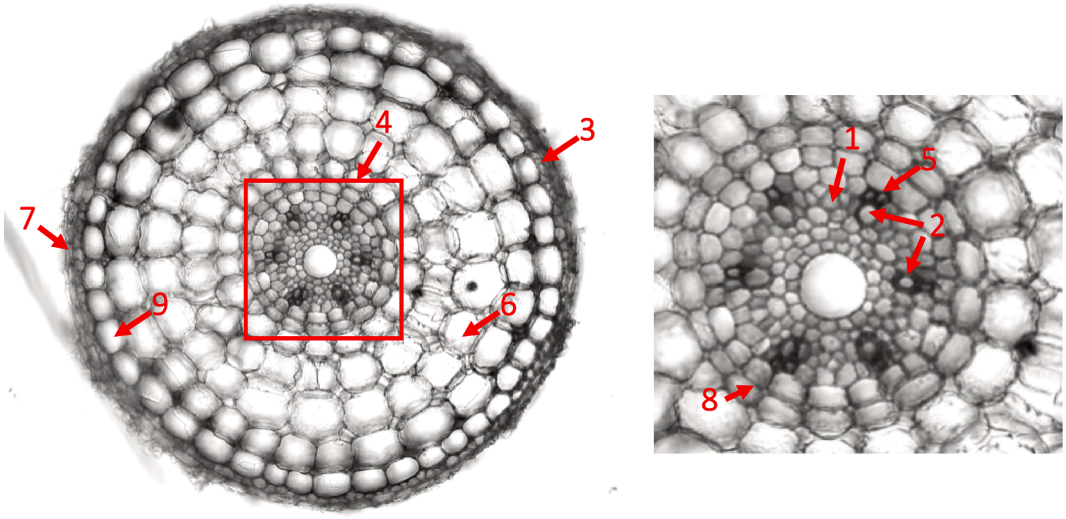

Fig. 1. Main anatomy of a cross-section of Oryza sativa Japonica root cross-section. 1) Phloem. 2) Xylems. 3) Sclerenchyma layer. 4) Stele. 5) Xylem-pole pericycle. 6) Cortex. 7) Epidermis. 8) Endodermis. 9) Exodermis.

To study the characterization of the natural fluorophores present on the rice root, a final image of a new root cross-section was acquired with only five excitation wavelengths (405, 470, 520, 570, 620 nm) and covering an emission range of 435–663 nm with 12 nm sampling interval and a bandwidth of 12 nm. The dwell time was 32 μs in all excitation wavelengths, except for 405 nm, where 15 μs were used.

All images had a pixel resolution of 450 × 450 nm^2.

3. Data treatment

This section covers the preprocessing applied to improve the signal-to-noise ratio of the fluorescence images and the description of the protocol based on the use of Multivariate Curve Resolution-Alternating Least Squares (MCR-ALS) for photobleaching and characterization studies using 3D and 4D fluorescence images.

3.1. Preprocessing

The images obtained have a high spatial resolution, with a pixel size of 450 × 450 nm^2, but the signal to noise ratio is too low for multivariate analysis. To address this issue, a binning of adjacent pixels (10 × 10) was done to improve the spectroscopic signal quality. Finally, the background was cropped.

In EEM measurements, the scattering produced by the Rayleigh emission has to be removed from the data, since it does not follow either bilinear nor trilinear responses. Thus, few emission channels close to the laser wavelength were set as not a number (NaN).

For the characterization study, the channel at excitation 405 nm and emission 591 nm showed a loss of signal, probably due to a problem with the detector. The channel was interpolated using the nearest emission wavelengths.

3.2. Multivariate Curve Resolution-Alternating least Squares (MCR-ALS)

Multivariate Curve Resolution-Alternating Least Squares [17] is an unmixing algorithm that decomposes the raw mixed information contained in an initial data set into a bilinear model of profiles related to their pure components, according to equation (1):

$$\mathbf{D} = \mathbf{C}\mathbf{S}^{\mathbf{T}} + \mathbf{E} \quad (1)$$

In a spectroscopic context, **D** is a table of raw mixture spectra and **S** and **C** are the matrices that contain the pure spectra and the related concentration profiles of the pure compounds, which can reproduce appropriately the information contained in the initial data set **D**. **E** is the variance unexplained by the bilinear model.

The MCR-ALS method works optimizing iteratively the **C** and **S** matrices via an alternating least squares procedure under constraints. An initial estimate of the matrix **C** or **S**, often obtained with a purest variable selection method, is required to start the optimization procedure. The constraints used are based on general mathematical or chemical properties that the profiles in **C** and **S** matrices naturally obey. The role of constraints is providing chemically meaningful profiles and decreasing the rotational ambiguity associated with the bilinear decomposition. The choice of the constraints is adapted to the nature of the profiles to be resolved and can be optionally applied per component and per mode (**C** and **S**). The iterative optimization is finished when a convergence criterion is reached, usually related to the fulfillment of a preset threshold value linked to the relative difference in lack of fit (see eq. 2) among consecutive iterations.

$$LOF(\%) = 100 \bullet \sqrt{\frac{\sum_{i,j} e_{i,j}^2}{\sum_{i,j} d_{i,j}^2}}$$

In the lack of fit expression, $d_{i,j}$ is an element of matrix **D** and $e_{i,j}$ from matrix **E**.

MCR-ALS has been applied in many diverse research fields and is particularly suitable for hyperspectral image analysis. The flexible data configurations and use of constraints of this algorithm allows the analysis of 3D and 4D HSIs [15,17,19–22]. The multiset modality of the method adapts to the simultaneous analysis of several related HSIs acquired with the same spectroscopic platform and to challenging image fusion scenarios where HSIs come from platforms differing in spectral dimensionality and spatial resolution.

The application of MCR-ALS to a single 3D or 4D fluorescence image implies transforming the initial image array into a data table and applying the suitable constraints. 3D images can be displayed as a cube where a full emission spectrum acquired at a fixed excitation wavelength is associated with each pixel of the sample surface. The image cube consists of two spatial pixel coordinates, x and y, and one spectral dimension, λ (see Fig. 2A). The cube can be easily unfolded into a data table by putting one pixel emission spectrum under the other. The **D** matrix obtained has a number of rows equal to the number of pixels ($x \times y$) and a number of columns equal to the number of emission wavelengths (λ). The bilinear model provided by MCR consists of a matrix with the pure emission spectra of the fluorophores in the sample (**S** matrix) and the related pixel concentration arrays (**C** matrix), which refolded according to the structure of the 2D sample surface provide the fluorophore distribution maps. The basic constraints that can be used in this resolution are non-negativity for both the concentration profiles and the pure emission spectra and spectra normalization in the **S** matrix.

4D images instead associate a 2D excitation-emission (EEM) landscape per every pixel. Therefore, the data table **D** is obtained by putting the vectorized 2D EEM landscape of every pixel, i.e., the concatenated emission spectra λ_{em} obtained at the different excitation wavelengths (λ_{ex_1} to λ_{ex_N}), one under the other (see Fig. 2B). The **D** matrix obtained has a number of rows equal to the number of pixels ($x \times y$) and a number of columns equal to the total number of emission channels in the vectorized EEM spectrum. The bilinear model provided by MCR consists of a matrix with a set of pure pixel concentration arrays, which are turned into fluorophore distribution maps, and a matrix with pure vectorized EEM landscapes related to each fluorophore (**S** matrix), which can be refolded into 2D EEM landscapes as well. All constraints mentioned for 3D images can be applied to 4D images. However, the nature of 2D EEM spectra allows for the application of the trilinearity constraint to matrix **S.** In plain words, the action of this constraint is forcing that all emission spectra within the EEM vectorized profile of a pure compound show the same shape across all the excitation wavelengths covered. Since the 2D EEM landscapes of fluorescence images show a systematic pattern of missing values when the excitation and emission ranges overlap, i.e., no emission fluorescence values are obtained if the emission wavelength is lower than the excitation wavelength, a dedicated implementation of the trilinearity constraint able to handle structures with missing values has been applied [23]. The three modes of the trilinear model linked to a 4D single image analysis by MCR-ALS would be the concentration and the emission spectra (explicit modes in the MCR decomposition) and the excitation mode (embedded in the vectorized EEM landscape).

An asset of MCR-ALS is the possibility to work with several related HSIs into a single multiset structure. For both 3D and 4D images, this can be easily accomplished by appending the blocks of spectral information of the different sample images (either single emission spectra in 3D images or vectorized 2D EEM landscapes in 4D images) one under the other. Such a multiset configuration is used in fluorophore characterization studies by analyzing multisets formed by images of different samples and the constraints used would be the same as for the analysis of single 3D and 4D images.

Multisets related to photobleaching studies deserve a special comment. As described in the introduction, the study of the photobleaching phenomenon can be easily carried out by analyzing simultaneously a set of fluorescence HSIs obtained on the same sample over time (see Fig. 3).

The nature of the photobleaching phenomenon allows taking advantage of the singular behavior of the fluorophores and the related

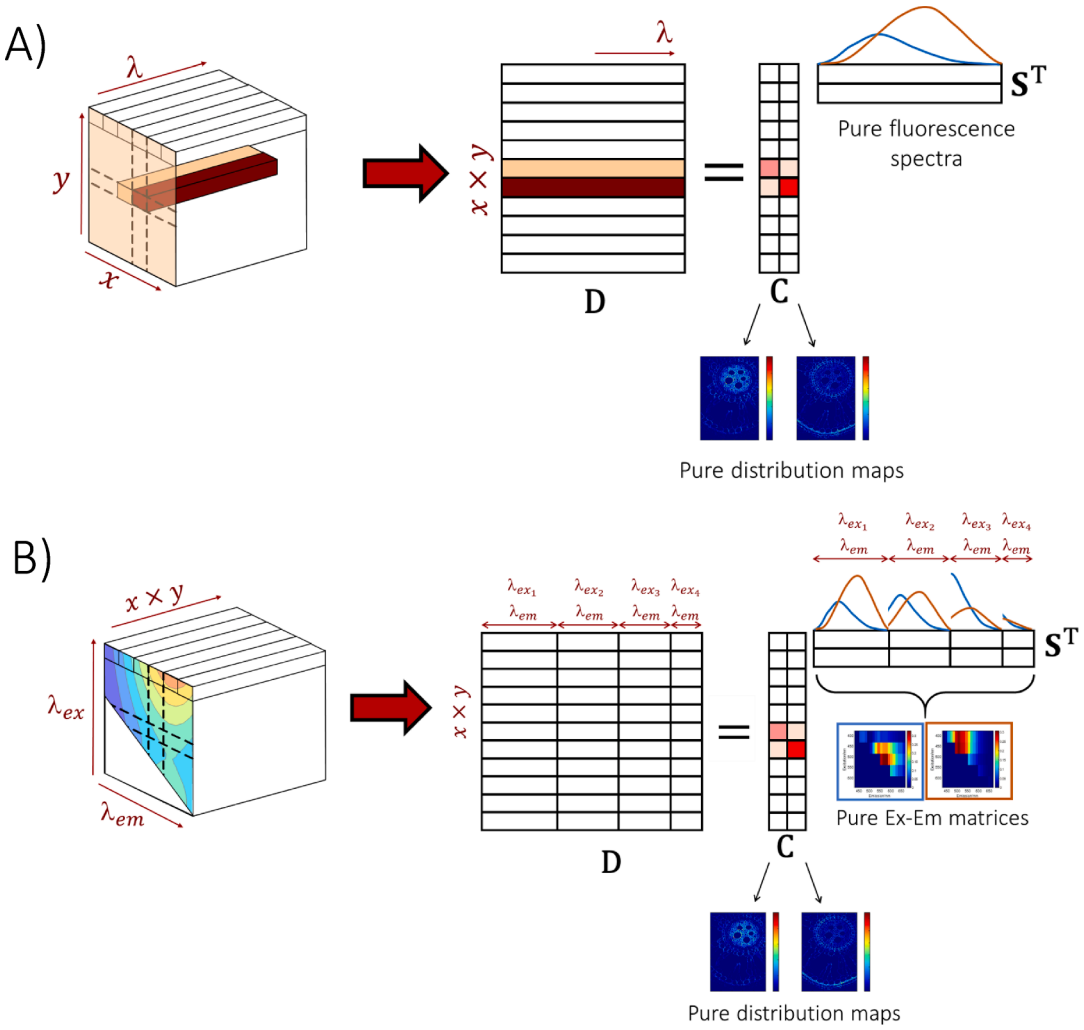

Fig. 2. A) MCR model for a 3D fluorescence image. B) MCR model for a 4D fluorescence image.

samples in the experiments performed. On the one hand, since the measurement is based on fluorescence spectroscopy, the shape of the emission spectra for every pure fluorophore remains invariant across the wavelength excitation range and/or across time and only the global signal intensity varies; on the other hand, since HSIs are collected on the same sample as a function of time, the shape of the concentration map of every fluorophore remains invariant across time and only the fluorescence intensity is modified because of photobleaching. These two facts allow a high flexibility in terms of data configuration and implementation of model constraints, as will be described below for studies carried out by using 3D and 4D images.

Fig. 3A shows the data arrangement and MCR model for a photobleaching study based on a time-series of 3D images. In this case, since the spatial structure of the concentration maps of every fluorophore is invariant over time and, hence, the shape of the related concentration profile, the blocks of spectral information from the different images are appended one beside the other forming a row-wise augmented multiset. As a consequence, the resulting MCR model obtained is formed by a single **C** matrix, which reflects the invariant shape of concentration profiles and, hence, of the related refolded maps of every fluorophore, and an augmented $\mathbf{S}^{\mathbf{T}}$ matrix, which contains in every row the concatenated emission spectra of a single fluorophore at the different photobleaching times studied. Other than non-negativity in the concentration and spectral profiles, trilinearity is applied to the $\mathbf{S}^{\mathbf{T}}$ matrix, forcing the shape of the emission spectrum of every pure fluorophore to remain constant at the different photobleaching times monitored. Finally, the pure decay signal of every fluorophore is obtained representing the area under the profile of each concatenated pure emission spectrum as a function of the related photobleaching time. In the case of photobleaching based on 3D images, the direction extended in time has been the spectral one because this mode was the least selective. Due to this fact, trilinearity could be applied and the pure spectra were resolved without ambiguity [17].

Photobleaching based on collecting 4D images over time required a different data configuration, shown in Fig. 3B). Every 4D acquired was unfolded as shown in Fig. 2B) and the blocks of information related to every photobleaching time were organized one under the other. The result is a row- and column-wise augmented multiset and the resulting MCR model will be formed by an augmented **C** matrix formed by the pixel concentration arrays (turned into concentration maps) linked to each photobleaching time studied and an augmented **S** matrix that has the same information as when a single 4D image is analyzed (see Fig. 2B). Adding to the non-negativity constraint, the trilinearity constraint has been used in the two directions of the MCR model. In the spectral direction, the adaptation of this constraint to handle missing values has been used. In the concentration direction, the classical implementation of trilinearity was applied forcing all concentration profiles (hence, maps) of the same fluorophore to have the same shape along time. The fluorescence decay profiles of every fluorophore can be subsequently obtained by integrating (summing) the values of the elements of the concentration profiles at every photobleaching time.

Looking carefully at the way photobleaching studies are done and

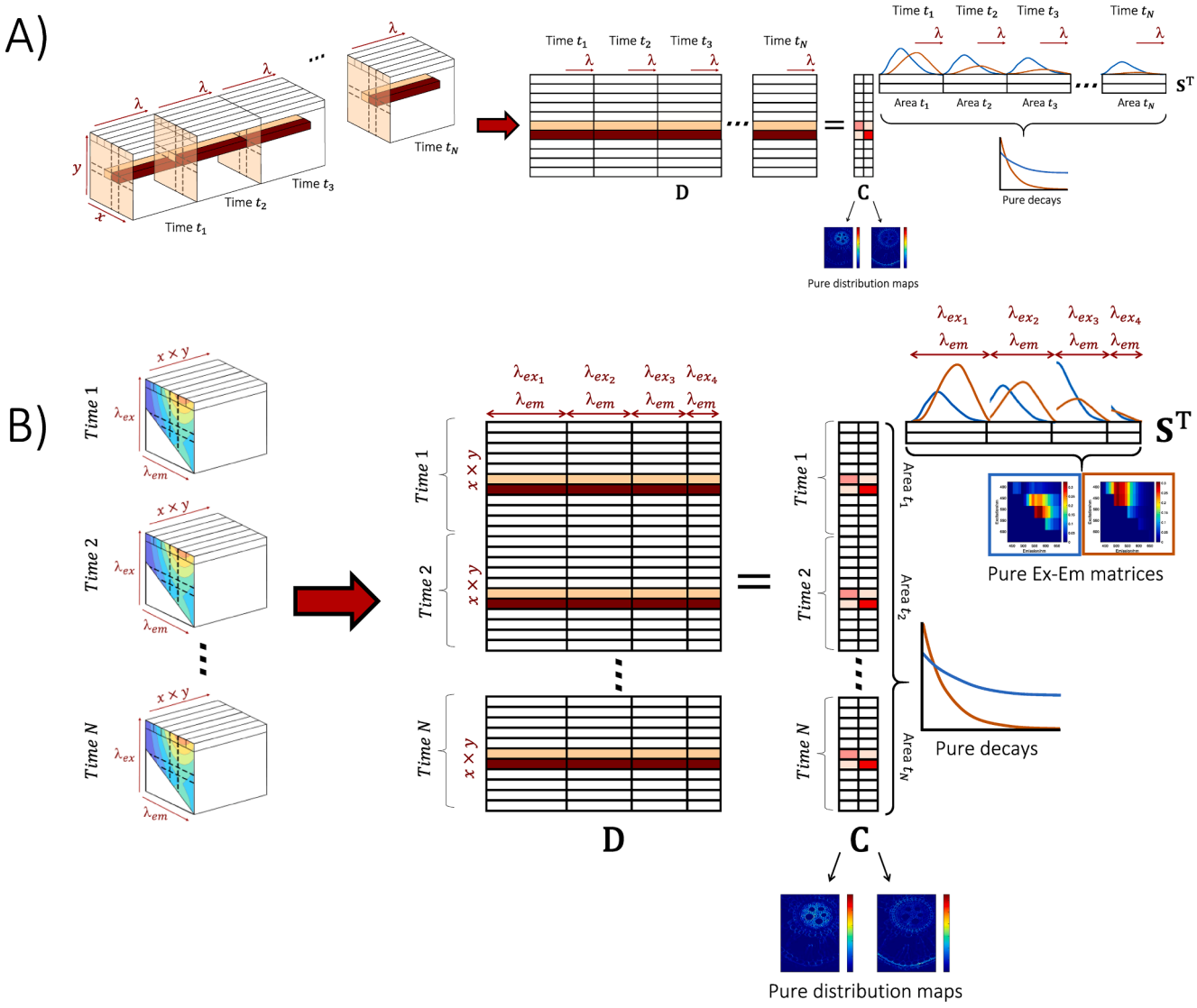

Fig. 3. A) Multiset configuration and related MCR model for a photobleaching experiment based on: A) 3D fluorescence images and B) 4D fluorescence images.

the way MCR analysis is performed, photobleaching studies based on 3D fluorescence images obey a trilinear model, where the three modes are the concentration profiles and the emission spectra (explicit MCR modes), and the decay profile mode (embedded in the set of emission spectra augmented over time). Analogously, photobleaching based on 4D fluorescence images obeys a quadrilinear model (see Fig. 3B), where the four modes are the concentration profiles and the emission spectra (explicit MCR modes), the excitation mode (embedded in the vectorized EEM landscape) and the decay profile mode (embedded in the set of concentration profiles). Thus, MCR provides a flexible framework for multilinear model implementation and, as a consequence of the use of these higher-order multilinear models, the fluorophore information can be recovered in a unique way.

3.3. Software

All in-house routines, scripts and analyses generated to preprocess and the analyze the data were performed using MATLAB 2021 (The Mathworks, Inc., Natick, MA).

4. Results and discussion

The photobleaching studies were performed by taking consecutive images (3D or 4D) on a single root cross-section over time under the same instrumental conditions and analyzing them by MCR-ALS. The results obtained in the study of the photobleaching effect helped to set the optimal image acquisition settings for the final characterization study of the fluorophores present in rice root samples. Table 1 shows a summary of the models obtained in all studies carried out. The nature, location and photobleaching decay of every component will be discussed in the following sections.

4.1. Photobleaching studies

For the results reported below, initial spectral estimates were calculated by a SIMPLISMA-based method [24]. Non-negativity was applied to **C** and **S**. Trilinearity constraint is often used and adapted depending on the context of the study, as will be described below. Convergence criterion was set to 10^{-6} % difference in lack of fit among consecutive iterations. After the MCR-ALS analysis, to recover the distribution maps at the initial high resolution, an extra least squares step

Table 1
Instrumental conditions and MCR-ALS results of each of the characterization experiments.

Photobleaching						
Dataset	Excitation range (nm)	Emission range (nm)	No. images (time step/min)	NC (*)	LOF (%)	Explained variance (%)
3D	405	432.5–597.5	6 (8)	3	10.7	98.9
4D	470–582	504–624	3 (12)	5	18.5	96.6
Characterization						
4D	405,470,520, 570,620	435–663	–	8	3.6	99.9

(*) NC: Number of components.

was performed using the optimal spectral profiles and the image data without binning.

4.1.1. 3D fluorescence images

The six 3D fluorescence images were concatenated as Fig. 3A. Trilinearity constraint was applied to force the emission shape to be the same for each component over the time. Three components were resolved (Fig. 4). The variance of the original data, i.e., the binned image (see section 3.1), is well explained by the MCR – ALS model (98.9%).

The first component found by MCR-ALS is significantly affected by photobleaching, losing 41% of the signal after 40 min of image acquisition. This component seems to be related to small vesicles (red color in Fig. S1), the cortex and the external part of the epidermis, with an emission maximum at 450 nm. The second component is present in the endodermis and the sclerenchyma layer of the epidermis (green color in Fig. S1). This component is less affected than the first one by photobleaching, having a loss of signal only of 6% after 40 min of image acquisition, with an emission maximum at 500 nm. Finally, the last component is specific of the inner part of the stele, where the cells are used to be more lignified (blue color in Fig. S1), with an emission maximum around 470 nm. The photobleaching affects even less this component than the previous ones, having a loss of signal of 3% after 40 min of imaging.

4.1.2. 4D fluorescence images

The three 4D fluorescence images were concatenated as in Fig. 3B into a single multiset. Trilinearity constraint was applied to force the concentration profile shape to be the same for each component over the time. On the other hand, the pure fluorescence profiles were forced to have the same shape across the excitations [23], resulting in a quadrilinear model. Convergence criterion was set to 10^{-6} % difference in lack of fit among consecutive iterations.

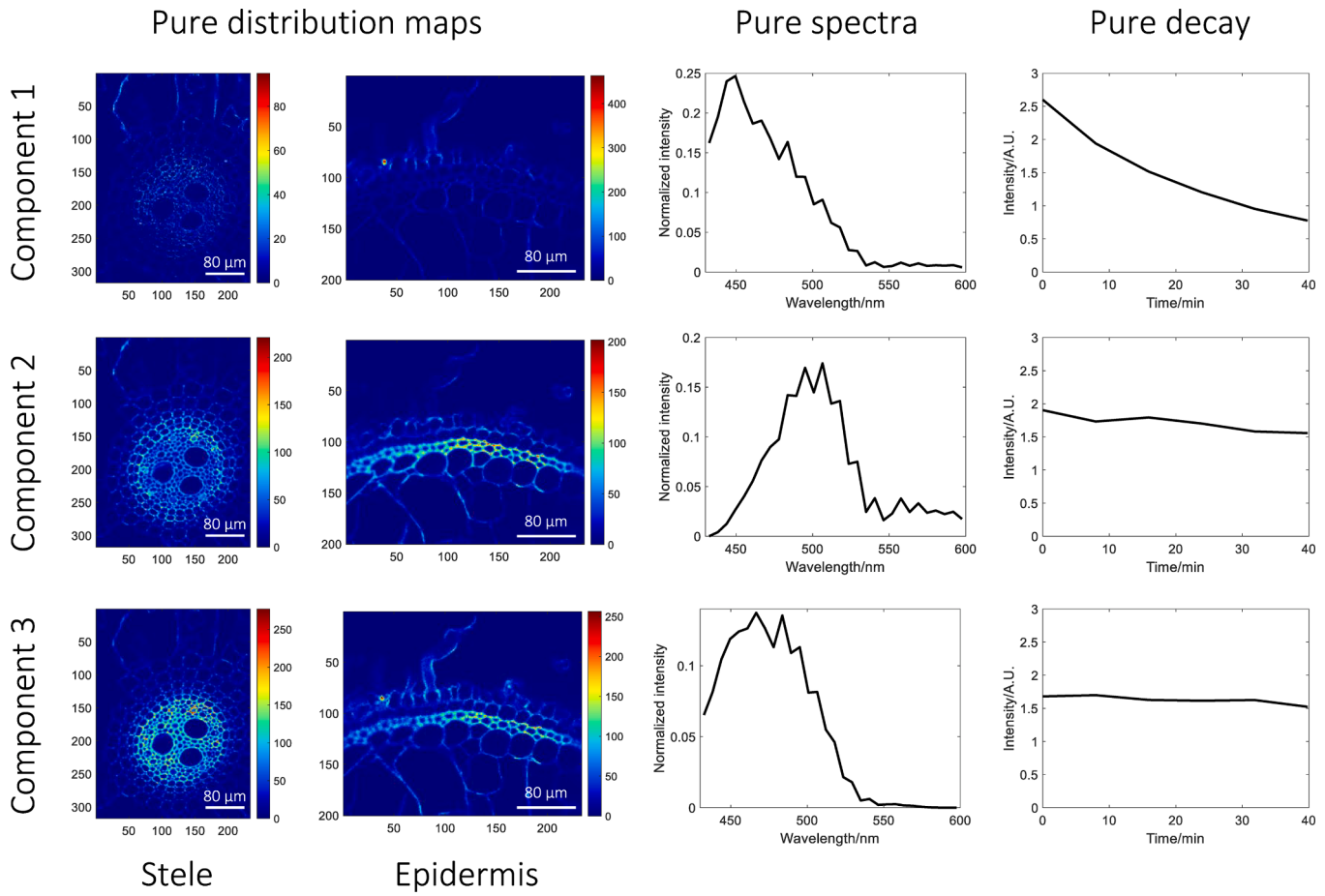

Fig. 4. MCR results obtained from the 3D photobleaching data. Plots from left to right: distribution maps (stele and epidermis ROIs), pure fluorescence emission spectra and pure photobleaching decay. Note that time 0 in the pure decay plots means the final time of acquisition of the first image acquired in the photobleaching experiment, i.e., 8 min.

Using MCR-ALS, five components were detected (Fig. 5), which explained 96.6% of the variance. In order to recover the distribution maps at the initial high resolution, an extra least squares step was performed using the optimal spectral profiles and the image data without binning.

Component 1 is related to an accumulation in the stele. The excitation maximum is around 480 nm, while the emission maximum is around 520 nm. There is no photobleaching phenomenon associated with this component. Component 2 is located in the endodermis and the sclerenchyma layer of the exodermis. This component has a similar excitation maximum than component 1, around 480 nm. However, the pure emission spectrum has a maximum around 530 nm. The photobleaching effect is significant for this component, with a loss of 55% of its signal in 24 min. Component 3 is specific of the sclerenchyma layer of the exodermis. The excitation maximum is around 530 nm and its emission around 570 nm. This component is affected by photobleaching as well, losing 11% of its intensity after 24 min of imaging. Component 4 appears on the cortex, but it has significant signal in the rest of the root, being a general component across the tissue. It has two different emission regions. The first one is located at an excitation of 500 nm and an emission of 540 nm. The second region is located at an excitation of 570 nm and an emission 620 nm, being a yellow–red fluorescence, in contraposition of the rest of components, located in the blue-green emission region. Finally, component 5 is the most shifted to the blue emission. Its excitation is 470 nm and the emission around 500 nm, and it is located in the phloem vessels and the sclerenchyma layer of the exodermis. This component seems to be almost unaffected by photobleaching, having a loss of signal around 4%.

The study of photobleaching in data sets formed by 3D and 4D fluorescence images using MCR-ALS has revealed that the photobleaching phenomenon is fluorophore-dependent and it is mandatory to perform an unmixing task of the image to properly characterize this behavior for the individual components of the sample. In the context of the rice root study, the results have shown that certain fluorophores present in the root tissue are sensitive to laser exposure at certain wavelengths, and their decay can significantly impact the quality of the measurement. Therefore, in order to accurately characterize the natural fluorophores present in the root tissue, it is important to minimize photobleaching effects. To achieve this, a strategy has been developed to reduce the number of excitation and emission channels to decrease the exposure time, while simultaneously increasing the bandwidth of the detector to increase the signal-to-noise ratio. This approach has allowed the acquisition of complete 4D images with a high signal-to-noise ratio in just 10 min, effectively minimizing the impact of photobleaching. It is clear that the effect of photobleaching must be considered on a per-component basis, as different fluorophores react differently to laser exposure.

4.2. Characterization study

Once the photobleaching phenomenon was confirmed in some components, the instrumental settings for the characterization of fluorescence components in root sections were tuned according to Section 2.2. The 4D hyperspectral image was unfolded as in Fig. 2B. Trilinearity constraint was applied to force the fluorescence emission profiles to have the same shape across the excitations. Using MCR-ALS, eight components were detected (Fig. 6), which explained 99.9% of the variance.

Fig. 7 displays the distribution maps of most of the biological components in false color, to highlight the differences among them. Component 1 (in red in Fig. 7A and B) appears on the pith of the root where the tissue is highly lignified, being more intense in the xylems and early xylems. It has an excitation maximum around 405 nm, while the emission maximum is around 480 nm. This compound could be attributed to lignin [25], specifically that which is related with lignified cells conforming the pith. Component 2 (in red in Fig. 7C) is related to the endodermis, but it has significant signal in the rest of the root, being a component located across all the tissues. Its excitation maximum is

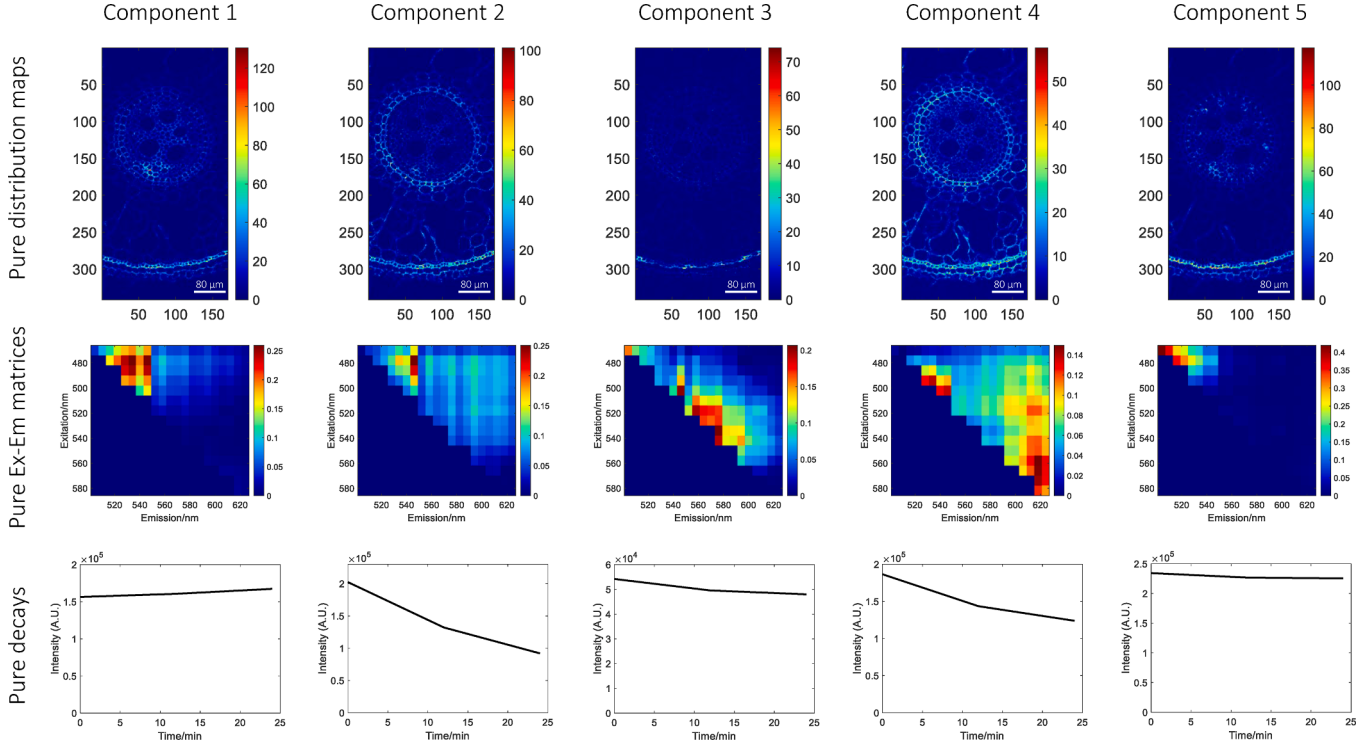

Fig. 5. MCR results obtained from the 4D photobleaching data. Plots from top to bottom: distribution maps, pure excitation-emission matrices and pure photobleaching decay. Note that time 0 in the pure decay plots means the final time of acquisition of the first image acquired in the photobleaching experiment, i.e., 12 min.

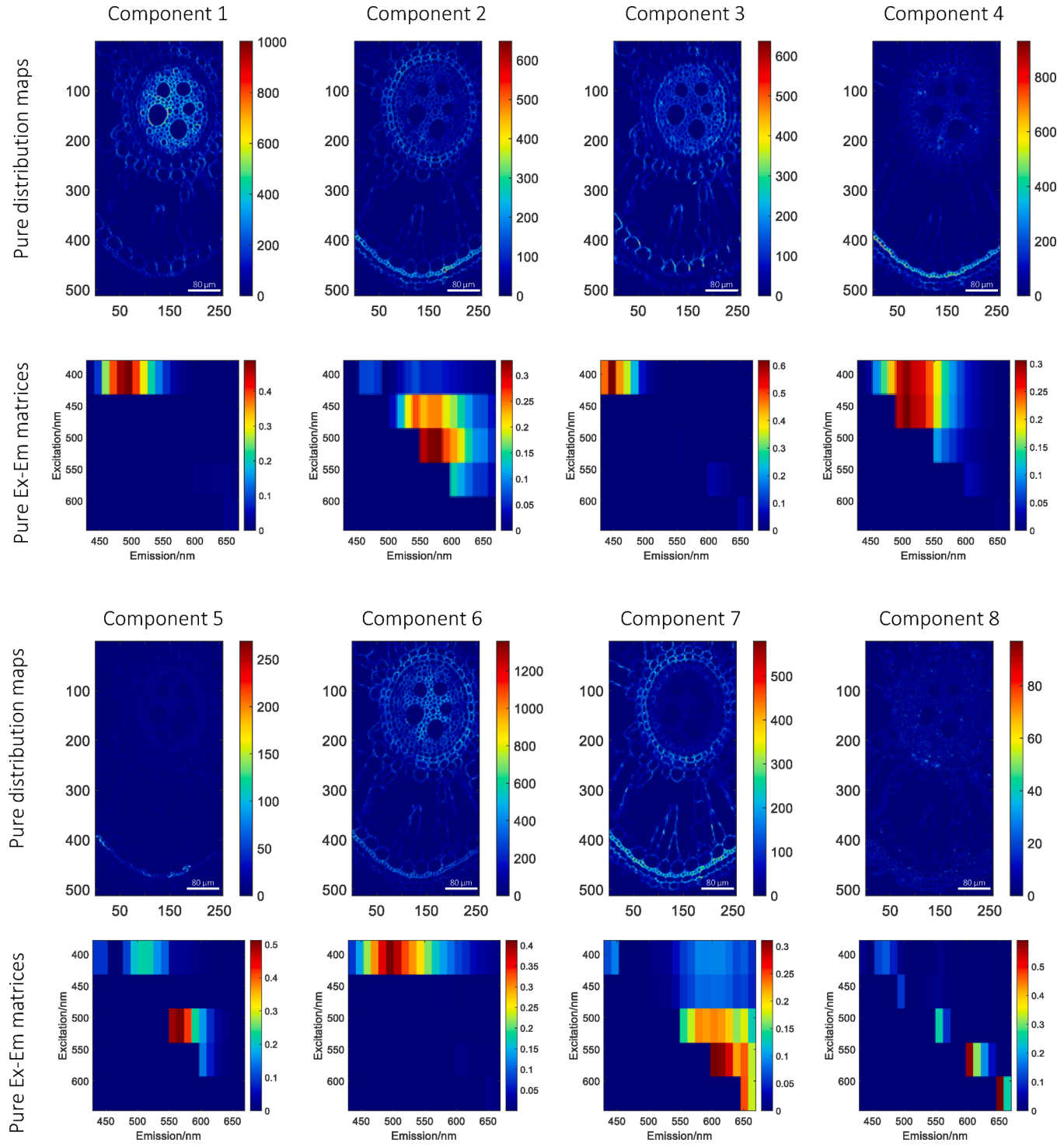

Fig. 6. MCR results for the characterization study performed using the 4D image. Distribution maps and pure EEM landscapes of the resolved components.

around 520 nm, while the emission is around 570 nm. Further investigation is needed to correctly characterize this component. Component 3 (in green in Fig. 7A and B) has an excitation of 405 nm and an emission around 440 nm, and it is located in the pericycle. It can be observed specifically in the phloem companion cells. To the knowledge of the authors, the fluorescence of the phloem companion cells has not been reported yet in rice roots. Component 4 (in blue in Fig. 7) is present in the sclerenchyma layer of the exodermis, but also in the xylem-pole pericycle. It can be observed as well where the Casparian strip should be located. This is a similar distribution found by Vishal, B. [26], which may indicate the presence of suberin. It has an excitation around 405–470 nm, while the emission is around 500 and 550 nm. Component 5 is specific of the sclerenchyma layer of the exodermis, having an excitation around 520 and an emission around 560 nm. Component 6 is located in all the root tissues, being characterized probably as a type of lignin not specific of any particular tissue. The excitation maximum is 405 while the emission is around 500 nm. Component 7 (in green in Fig. 7C) appears in the endodermis, the exodermis and the epidermis. In addition, small vesicles inside some vessels are specifically related to this component. A reasonable hypothesis is that these vesicles can be

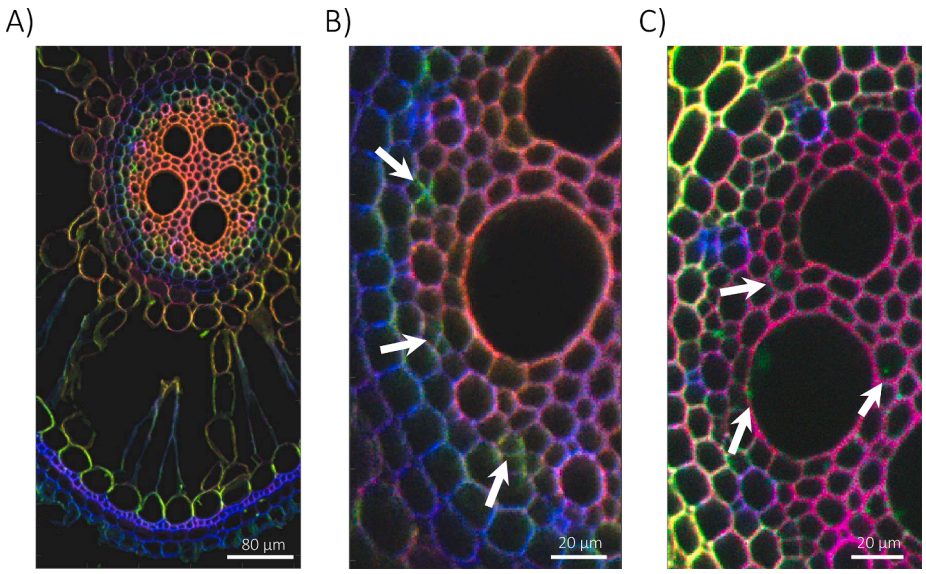

Fig. 7. Overlap of normalized distribution and color-saturated maps from the MCR-ALS analysis shown in Fig. 6 in false color. A) Red, green and blue are components 1, 3 and 4, respectively. B) Detailed zoom of the pith. C) Red, green and blue are components 2, 7 and 4, respectively.

related to silica bodies [27]. Its excitation is around 570 nm and its emission around 620 nm. Finally, the Component 8 is an artifact due to Rayleigh scattering.

Thus, thanks to the application of MCR-ALS to 3D and 4D images and to the previous study of the photobleaching phenomenon, the optimal image acquisition parameters to minimize photobleaching and improve the overall quality of data obtained from fluorescence imaging of root tissue could be obtained. Improving the signal-to-noise ratio (SNR) of fluorescence data, MCR-ALS could improve the detection and unmixing of natural fluorescence compounds present in root tissue, as it is reflected in Table 1, i.e., the number of components detected and the explained variance by the MCR model increased significantly even if the characterization experiment took only 10 min. In this context, the use of MCR-ALS also enabled to identify previously undetected compounds, which can provide valuable insights into the biology and physiology knowledge of plants.

5. Conclusions

The photobleaching phenomenon needs to be adequately described to guide a proper fluorescence image acquisition that allows detecting and characterizing all fluorophores present in samples while minimizing sample photodamage.

To do so, sets of 3D or 4D fluorescence images need to be acquired over time and be analyzed simultaneously. Characterization of the photobleaching phenomenon of a sample requires considering that this phenomenon is fluorophore-specific and some compounds may show a high signal decay while others may be almost invariant along time. To assist in this individual characterization, the unmixing methodology MCR-ALS is particularly suitable. Owing to the flexibility in the use of model constraints, pure fluorophore specificities like the invariance of the shape of maps and of pure excitation-emission spectra during photobleaching can be appropriately considered. To do so, trilinearity constraints applied in the maps and/or spectral directions and inclusion of model constraint variants that can handle the presence of systematic patterns of absent values in 2D excitation-emission landscapes is exploited. Thus, photobleaching in 3D and 4D images can be adequately described with dedicated trilinear and quadrilinear models, respectively, always providing concentration and spectral profiles and, most important, photobleaching decay curves, for every resolved fluorophore. Additionally, the multilinear nature of the models applied ensures unique solutions.

Once the photobleaching phenomenon is characterized, strategies like selecting few excitation channels to build sufficiently informative 4D fluorescence images with a limited sample exposure time ensure the characterization of all fluorescent compounds despite their different sensitivity to photobleaching.

The presented approach has been shown to be particularly suitable for challenging biological samples, with a high number of spectrally and spatially overlapped fluorescent compounds with very different photobleaching behavior, and can be extended to any kind of samples containing natural fluorescent compounds or fluorophores used for staining purposes.

CRediT authorship contribution statement

Adrián Gómez-Sánchez: Conceptualization, Methodology, Software, Formal analysis, Investigation, Data curation, Visualization, Writing - original draft, Writing - review & editing. **Iker Alburquerque Alvarez:** Formal analysis, Investigation, Data curation, Visualization, Writing - review & editing. **Pablo Loza-Alvarez:** Resources, Funding acquisition, Writing - review & editing. **Cyril Ruckebusch:** Resources, Funding acquisition, Writing - review & editing. **Anna de Juan:** Conceptualization, Methodology, Formal analysis, Resources, Supervision, Project administration, Funding acquisition, Writing - original draft, Writing - review & editing.

Declaration of Competing Interest

The authors declare that they have no known competing financial interests or personal relationships that could have appeared to influence the work reported in this paper.

Data availability

Data will be made available on request.

Acknowledgements

A. G.-S. and A.J. acknowledge financial support from the Spanish government Project PID 2019-1071586B-IOO and the Catalan government (2021 SGR 00449). A. G.-S. acknowledges scholarships from the MOBLILEX U Lille program and from the Santander bank.

PL-A acknowledge the Spanish Ministerio de Economía y

Competitividad (MINECO) through the “Severo Ochoa” program for Centres of Excellence in R&D (CEX2019-000910-S [MCIN/AEI/10.13039/501100011033]), Fundació Privada Cellex, Fundació Mir-Puig. Generalitat de Catalunya through CERCA program; Excellent recognized group 2021 SGR 01456 by the Departament de Recerca i Universitats de la Generalitat de Catalunya”and Laserlab-Europe EU-H2020 GA no. 871124.

Appendix A. Supplementary data

Supplementary data to this article can be found online at https://doi.org/10.1016/j.microc.2023.108899.

References

[1] B. Park, R. Lu (Eds.), Hyperspectral imaging technology in food and agriculture, Springer, Berlin, Germany, 2015.
[2] A. Gowen, C. Odonnell, P. Cullen, G. Downey, J. Frias, Hyperspectral imaging–an emerging process analytical tool for food quality and safety control, Trends Food Sci. Technol. 18 (12) (2007) 590–598.
[3] G. Lu, B. Fei, Medical hyperspectral imaging: a review, J. Biomed. Opt. 19 (1) (2014) 010901.
[4] M.A. Calin, S.V. Parasca, D. Savastru, D. Manea, Hyperspectral imaging in the medical field: Present and future, Appl. Spectrosc. Rev. 49 (6) (2014) 435–447.
[5] B. Fei, Hyperspectral imaging in medical applications. En Data Handling in Science and Technology, Elsevier, 2019, pp. 523–565.
[6] J.M. Amigo, J. Cruz, M. Bautista, S. Maspoch, J. Coello, M. Blanco, Study of pharmaceutical samples by NIR chemical-image and multivariate analysis, TrAC Trends Anal. Chem. 27 (8) (2008) 696–713.
[7] C. Gendrin, Y. Roggo, C. Collet, Pharmaceutical applications of vibrational chemical imaging and chemometrics: a review, J. Pharm. Biomed. Anal. 48 (3) (2008) 533–553.
[8] H.C. Goicoechea, A.C. Olivieri, R. Tauler, Application of the correlation constrained multivariate curve resolution alternating least-squares method for analyte quantitation in the presence of unexpected interferences using first-order instrumental data, Analyst 135 (3) (2010) 636–642.
[9] V. Olmos, L. Benítez, M. Marro, P. Loza-Alvarez, B. Piña, R. Tauler, A. de Juan, Relevant aspects of unmixing/resolution analysis for the interpretation of biological vibrational hyperspectral images, TrAC Trends Anal. Chem. 94 (2017) 130–140.
[10] K. Fackler, L.G. Thygesen, Microspectroscopy as applied to the study of wood molecular structure, Wood Sci. Technol. 47 (1) (2013) 203–222.
[11] N. Gierlinger, M. Schwanninger, Chemical imaging of poplar wood cell walls by confocal Raman microscopy, Plant Physiol. 140 (4) (2006) 1246–1254.
[12] M.J. Rust, M. Bates, X. Zhuang, Sub-diffraction-limit imaging by stochastic optical reconstruction microscopy (STORM), Nat. Methods 3 (10) (2006) 793–796.
[13] S.W. Hell, J. Wichmann, Breaking the diffraction resolution limit by stimulated emission: stimulated-emission-depletion fluorescence microscopy, Opt. Lett. 19 (11) (1994) 780–782.
[14] S. Hugelier, J.J. de Rooi, R. Bernex, S. Duwé, O. Devos, M. Sliwa, P. Dedecker, P.H. C. Eilers, C. Ruckebusch, Sparse deconvolution of high-density super-resolution images, Sci. Rep. 6 (1) (2016).
[15] A. Gómez-Sánchez, M. Marro, M. Marsal, P. Loza-Alvarez, A. de Juan, 3D and 4D image fusion: coping with differences in spectroscopic modes among hyperspectral images, Anal. Chem. 92 (14) (2020) 9591–9602.
[16] R.A. Hoebe, C.H. Van Oven, T.W.J. Gadella, P.B. Dhonukshe, C.J.F. Van Noorden, E.M.M. Manders, Controlled light-exposure microscopy reduces photobleaching and phototoxicity in fluorescence live-cell imaging, Nat. Biotechnol. 25 (2) (2007) 249–253.
[17] A. De Juan, R. Tauler, Multivariate Curve Resolution: 50 years addressing the mixture analysis problem–A review, Anal. Chim. Acta 1145 (2021) 59–78.
[18] J. Rebouillat, A. Dievart, J.L. Verdeil, J. Escoute, G. Giese, J.C. Breitler, P. Gantet, S. Espeout, E. Guiderdoni, C. Périn, Molecular genetics of rice root development, Rice 2 (1) (2009) 15–34.
[19] Anna De Juan, Multivariate curve resolution for hyperspectral image analysis, in: En Data Handling in Science and Technology, Elsevier, 2019, pp. 115–150.
[20] S. Hugelier, O. Devos, C. Ruckebusch, On the implementation of spatial constraints in multivariate curve resolution alternating least squares for hyperspectral image analysis, J. Chemom. 29 (10) (2015) 557–561.
[21] S. Hugelier, et al., Application of a sparseness constraint in multivariate curve resolution–alternating least squares, Anal. Chim. Acta 1000 (2018) 100–108.
[22] A. de Juan, M. Maeder, T. Hancewicz, R. Tauler, Use of local rank-based spatial information for resolution of spectroscopic images, J. Chemometrics: J. Chemometrics Soc. 22 (5) (2008) 291–298.
[23] A. Gómez-Sánchez, I. Alburquerque, P. Loza-Álvarez, C. Ruckebusch, A. de Juan, The trilinear constraint adapted to solve data with strong patterns of outlying observations or missing values, Chemom. Intel. Lab. Syst. 231 (2022) 104692.
[24] W. Windig, D.A. Stephensom, Self-modeling mixture analysis of second-derivative near-infrared spectral data using the SIMPLISMA approach, Anal. Chem. 64 (22) (1992) 2735–2742.
[25] L. Donaldson, N. Williams, Imaging and spectroscopy of natural fluorophores in pine needles, Plants 7 (1) (2018) 10.
[26] B. Vishal, et al., Os TPS 8 controls yield-related traits and confers salt stress tolerance in rice by enhancing suberin deposition, New Phytol. 221 (3) (2019) 1369–1386.
[27] N. Zexer, R. Elbaum, A. Lux, Unique lignin modifications pattern the nucleation of silica in sorghum endodermis, J. Exp. Bot. 71 (21) (2020) 6818–6829.